Interface Reconstruction from Ruddlesden–Popper Structures Impacts Stability in Lead Halide Perovskite Solar Cells

Carlo Andrea Riccardo Perini, Esteban Rojas-Gatjens, Magdalena Ravello, Andrés-Felipe Castro-Mendez, Juanita Hidalgo, Yu An, Sanggyun Kim, Barry Lai, Ruipeng Li, Carlos Silva-Acuña, and Juan-Pablo Correa-Baena*

The impact of the bulky-cation-modified interfaces on halide perovskite solar cell stability is underexplored. In this work, the thermal instability of the bulky-cation interface layers used in the state-of-the-art solar cells is demonstrated. X-ray photoelectron spectroscopy and synchrotron-based grazing-incidence X-ray scattering measurements reveal significant changes in the chemical composition and structure at the surface of these films that occur under thermal stress. The changes impact charge-carrier dynamics and device operation, as shown in transient photoluminescence, excitation correlation spectroscopy, and solar cells. The type of cation used for surface treatment affects the extent of these changes, where long carbon chains provide more stable interfaces. These results highlight that prolonged annealing of the treated interfaces is critical to enable reliable reporting of performances and to drive the selection of different bulky cations.

1. Introduction

Bulky organic cations—too big to form a corner-sharing octahedra metal halide perovskite—are widely used to reduce non-

C. A. R. Perini, M. Ravello, A.-F. Castro-Mendez, J. Hidalgo, Y. An, S. Kim, C. Silva-Acuña, J.-P. Correa-Baena
School of Materials Science and Engineering
Georgia Institute of Technology
Atlanta, GA 30332, USA
E-mail: jpcorrea@gatech.edu
E. Rojas-Gatjens, C. Silva-Acuña
School of Chemistry and Biochemistry
Georgia Institute of Technology
Atlanta, GA 30332, USA
B. Lai
Advanced Photon Source
Argonne National Laboratory
9700 Cass Avenue, Lemont, IL 60439, USA
R. Li
National Synchrotron Light Source II (NSLS-II)
Brookhaven National Laboratory
Upton, NY 11973, USA
C. Silva-Acuña
School of Physics
Georgia Institute of Technology
Atlanta, GA 30332, USA

The ORCID identification number(s) for the author(s) of this article can be found under https://doi.org/10.1002/adma.202204726.

radiative recombination at interfaces in high-performance metal halide perovskite photovoltaics. Despite numerous reports of performance enhancement, only a few studies have investigated the actual structure and structural stability of the interface treated with bulky cations.[1–4] Bulky organic salts, generally halides, have been reported to interact with point defects at the perovskite surfaces and to introduce a tunneling junction with the charge extraction layers, decreasing nonradiative recombination.[1] Such salts have been used to enable power conversion efficiencies (PCEs) up to 25.5% in solar cells based on halide perovskite films.[5,6] Bulky organic cations are frequently embedded at the perovskite and charge-transport-layer interface by deposition on already formed perovskite films, to create a uniform layer thin enough to avoid transport losses. Depending on the size, the deposition of bulky cations can lead to a reconstruction to lower structural dimensionality of the treated perovskite interface.[7]

While the passivation approach has been used widely, it is still unclear when the rearrangement of the interface occurs, and whether it is beneficial or if it should be prevented, with different groups reporting contrasting results.[1,5,6] The reconstruction of the treated interface during device operation, particularly in combination with thermal stress, could consequently result in PCE loss and shortened solar cell lifetimes, which have not been studied. In this contribution, we look at the evolution in the chemical and structural composition of the interface layer when exposed to thermal stress to understand its stability and the impact these changes have on device performance. We combine synchrotron-based grazing-incidence wide-angle X-ray scattering (GIWAXS), X-ray photoelectron spectroscopy (XPS), scanning electron microscopy (SEM), and optical spectroscopy measurements, such as transient photoluminescence (trPL) and excitation correlation spectroscopy (ECPL), to understand how the evolution in the structure, chemical composition, and microstructure of the interface induced by thermal stress impacts recombination dynamics in perovskite solar cells.

Our findings demonstrate that the passivation molecules deposited at the interface slowly permeate the perovskite film under thermal stress, impeding charge extraction and increasing nonradiative recombination. A clear correlation between the

**ADVANCED
SCIENCE NEWS**

www.advancedsciencenews.com

**ADVANCED
MATERIALS**

www.advmat.de

annealing of bulky cation-treated perovskite films and lower PCE is observed if the treated films are incorporated in n-i-p solar cells. The drop in PCE is also found when devices are exposed to long-term stability testing under 1 Sun equivalent illumination at 55 °C, a temperature of interest for photovoltaics operation. Notably, no abrupt performance decay is observed when devices are kept at room temperature during aging, which underlines the importance of testing at high temperature the solar cells comprising surface-treated perovskite films. The fast changes demonstrated by some of the most promising cations at the perovskite crystal surface show that these molecular surface modifiers can be detrimental to long-term device operation. This highlights the need for new molecules able to passivate the defects at the perovskite surface without diffusing and reconstructing the perovskite bulk and for understanding what factors drive the evolution of the interface.

2. Results and Discussion

2.1. Design of the Experiment

To understand how bulky organic salts impact the optoelectronic properties and stability of halide perovskite films, we deposited triple cation lead mixed halide layers, of approximate composition in solution $Cs_{0.06}FA_{0.79}MA_{0.16}PbBr_{0.49}I_{2.52}$ (here referred to as CsFAMA, where MA is methylammonium and FA is formamidinium). We modified the top surface of these films with organic salts containing the same number of carbons and based on a phenyl group or a linear chain, such as phenethylammonium iodide (PEAI), octylammonium iodide (OAI), and octylammonium bromide (OABr), which have been used for defect passivation in high-performance perovskite optoelectronics.[5,8–10] The treated samples were then thermally annealed at 100 °C for different time durations (0, 10, 40 min). A schematic of the different treatments and the solar cell stack used in this work is presented in **Figure 1**a. We highlight that the annealing conditions chosen in this work are not ideal for industrial production, and do not have the purpose of maximizing efficiency but to evaluate the stability of the interface treated with bulky cations, accelerating transformative dynamics happening at the interface.

2.2. Heat Drives the Reconstruction of the Bulky-Cation Interface

We began our investigation by monitoring with XPS the evolution in chemical composition of the treated perovskite surface
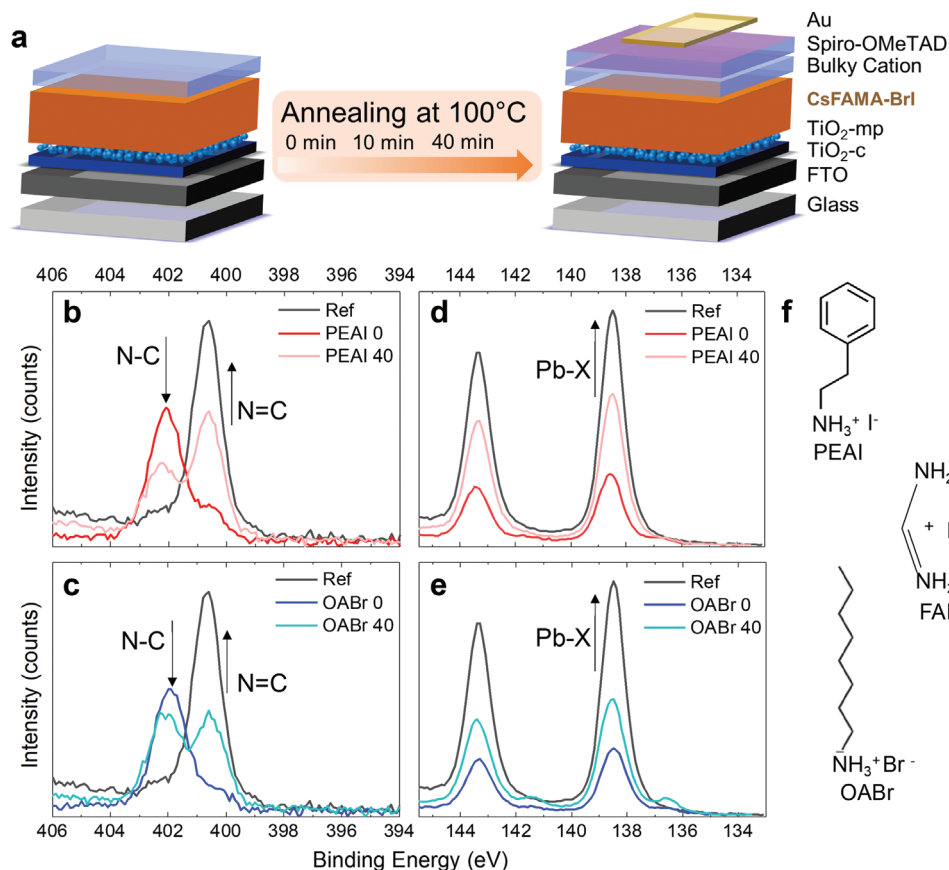

Figure 1. Compositional evolution under thermal stress of CsFAMA with the addition of a bulky cation layer. a) Solar cell architecture used in this work. The layers stack is presented on the right. The bulky cation layer of PEAI, OAI, or OABr (shown in blue) is annealed before introducing the spiro-OMeTAD and Au layers. b,c) XPS of N1s and d,e) Pb4f signals for metal halide perovskite films treated with PEAI (b,d) or OABr (c,e). The pristine CsFAMA film spectrum is reported in black. The 0 and 40 after the cation name in the legend are the annealing times in minutes, at 100 °C. f) Molecular structures of the cations used in this study.

**ADVANCED
SCIENCE NEWS**

www.advancedsciencenews.com

**ADVANCED
MATERIALS**

www.advmat.de

induced by annealing. The XPS elemental scans for N1s and Pb4f of the untreated film, labeled as "Ref", and of the perovskite treated with PEAI and OABr are presented in Figure 1b–e. The N1s and Pb4f scans for the PEAI-treated film annealed for 10 min and the OAI-treated films are presented in Figure S1 in the Supporting Information. The XPS scans for C1s, I3d, Br3d, Cs3d, O1s of PEAI, OABr, and OAI-treated films are presented in Figure S2 in the Supporting Information. Table S1 in the Supporting Information summarizes the approximate surface composition of the different films as extracted by the peak fits of the elemental scans reported in Figure S3 in the Supporting Information. A comparison of the N1s peak area of FA and MA for the reference film, C=N at 400.6 eV (FA) and C−N at 402.4 eV (MA), reveals an excess of FA and a deficiency in MA at the surface with respect to the starting solution composition, as quantified in Table S1 in the Supporting Information.[11] The N/Pb elemental ratio (N1s peaks/Pb4f Pb-X peak at 138.5 eV, where X is a halide) denotes the presence of an excess of organics, in agreement with previous reports detailing the tendency of FAI to accumulate at the exposed perovskite interface.[12,13]

The signatures of the organic cations, whose molecular structures are reported in Figure 1f, dominate the XPS surface spectrum of the perovskite films treated with PEAI and OABr before annealing (labeled PEAI 0, OABr 0). The N1s C−N peak intensity is enhanced significantly, which is attributed to the amine group of the bulky cations, along with a reduction in the C=N peak of FAI in Figure 1b,c. The C1s C−C and C−N peak intensities also increase with respect to the untreated perovskite film, and a broad π–π* satellite characteristic of aromatic compounds appears at 292 eV in the C1s elemental scan of PEAI-treated films in Figure S2 in the Supporting Information.[14] At the same time, the intensity of the Pb-X peak in Figure 1d,e—used as a marker for the presence of a metal halide Ruddlesden–Popper (RP) phase at the top surface—is suppressed, suggesting a top interface composed mostly of organic molecules. Signals from FA and Cs appear strongly reduced, yet still visible in Figure 1b,c and Figure S2 in the Supporting Information, which could be ascribed to incomplete coverage of the PEAI or OABr layer or to an X-ray penetration depth larger than the organic layer thickness. The Pb, Cs, and FA signals could al be generated by an RP layer beginning to form via the exchange of cations with the bottom perovskite film. Interestingly, the amount of iodine at the surface decreases, and the signal from bromine increases in all treated films with respect to the reference regardless of which halide was added during the bulky cation treatment, as shown in Figure S2 and Table S1 in the Supporting Information. Such trend suggests higher stability of Br-rich surfaces after introducing the bulky cations.

To test the stability of the interface treated with PEAI and OABr, we annealed the films at 100 °C, to accelerate changes in the structure at the surface. The XPS spectra of freshly deposited PEAI 0 and OABr 0 were compared with those that were annealed for 40 min after deposition on the perovskite film (here referred to as PEAI 40, OABr 40, respectively). The spectra presented in Figure 1b,c demonstrate how thermal stress leads to a decrease in the N1s C−N peak intensity associated with the PEA and OA cations and to an increase in the C=N FA signal. The decrease in intensity of the C−N signal is to be ascribed

to the diffusion of the PEA cation and not to loss of MA from the surface induced by annealing, as corroborated by comparing the XPS of untreated CsMAFA films post-treated with an extra 40 min of annealing at 100 °C (Figure S4, Supporting Information). Concurrently, the intensity of the Pb4f Pb-X signal increases, hinting at the conversion of the top interface to an RP structure or back to the original perovskite phase. The transition to this intermixed state happens relatively fast and is almost completed within the first 10 min of annealing in the case of PEAI, as shown in Figure S1 in the Supporting Information. Extending the annealing from 10 to 40 min produced only minor changes. The PEA (N1s N−C)/Pb4f ratio decreases by only 10%, in contrast to the 74% reduction observed within the first 10 min of annealing in Table S1 in the Supporting Information. For the OABr-treated films, a peak appears in the Pb4f elemental scan at 136.6 eV, attributed to the formation of Pb_0. The peak becomes more intense after annealing and might be related to the degradation in vacuum reported for RP phases.[15] An oxygen peak is visible in the O1s elemental scan of the CsFAMA reference (533 eV, C−O bond), which disappears in all treated films, in agreement with previous reports on the water and oxygen barrier effect exerted by bulky-cation-treated interfaces.[16,17] The interface also evolves at temperatures lower than 100 °C, as shown in Figure S5 in the Supporting Information. 40 minutes of annealing of the PEAI layer at 85 °C produce almost the same evolution in interface composition of the annealing at 100 °C. Instead, annealing at 65 °C does not produce significant changes with respect to the untreated film, suggesting that the surface transformation is either prevented or significantly slowed down at such temperature.

To explain if the changes in surface stoichiometry observed by XPS before and after the thermal treatment are associated with microstructural changes and with the formation of an RP structure, we performed SEM and synchrotron-based GIWAXS measurements on the deposited films. The SEM images in **Figure 2**a,c,e,g,i compare the morphology of PEAI and OABr-treated samples with and without annealing to the reference CsFAMA film. The introduction of the bulky cations makes it difficult to image the grain boundaries of the perovskite layer (Figure S6, Supporting Information). As a result, films with surface treatment and with no post-annealing were difficult to image in the SEM, particularly for the OA cation samples, as seen by comparing the PEAI 0-treated film in Figure 2a, the OABr 0 in Figure 2e, and the untreated reference in Figure 2i (see Figure S7, Supporting Information for OAI-treated films). The challenge in obtaining a sharp image for the treated layers is attributed to the formation of a thin amorphous/insulating organic layer on top of the CsFAMA surface. After 40 min of annealing, in Figure 2c, the image becomes more crisp for PEAI, which could be associated with the diffusion of the bulky cations and crystallization of RP phases. In contrast, for OABr in Figure 2g, focus in the SEM images is difficult to achieve even after the annealing step. GIWAXS of the films was taken to correlate changes in the microstructure observed by SEM with the formation of RP structures on the top surfaces of the films. The complete set of GIWAXS measurements for the films is presented in Figure S8 in the Supporting Information. Samples treated with PEAI in Figure 2b show the formation
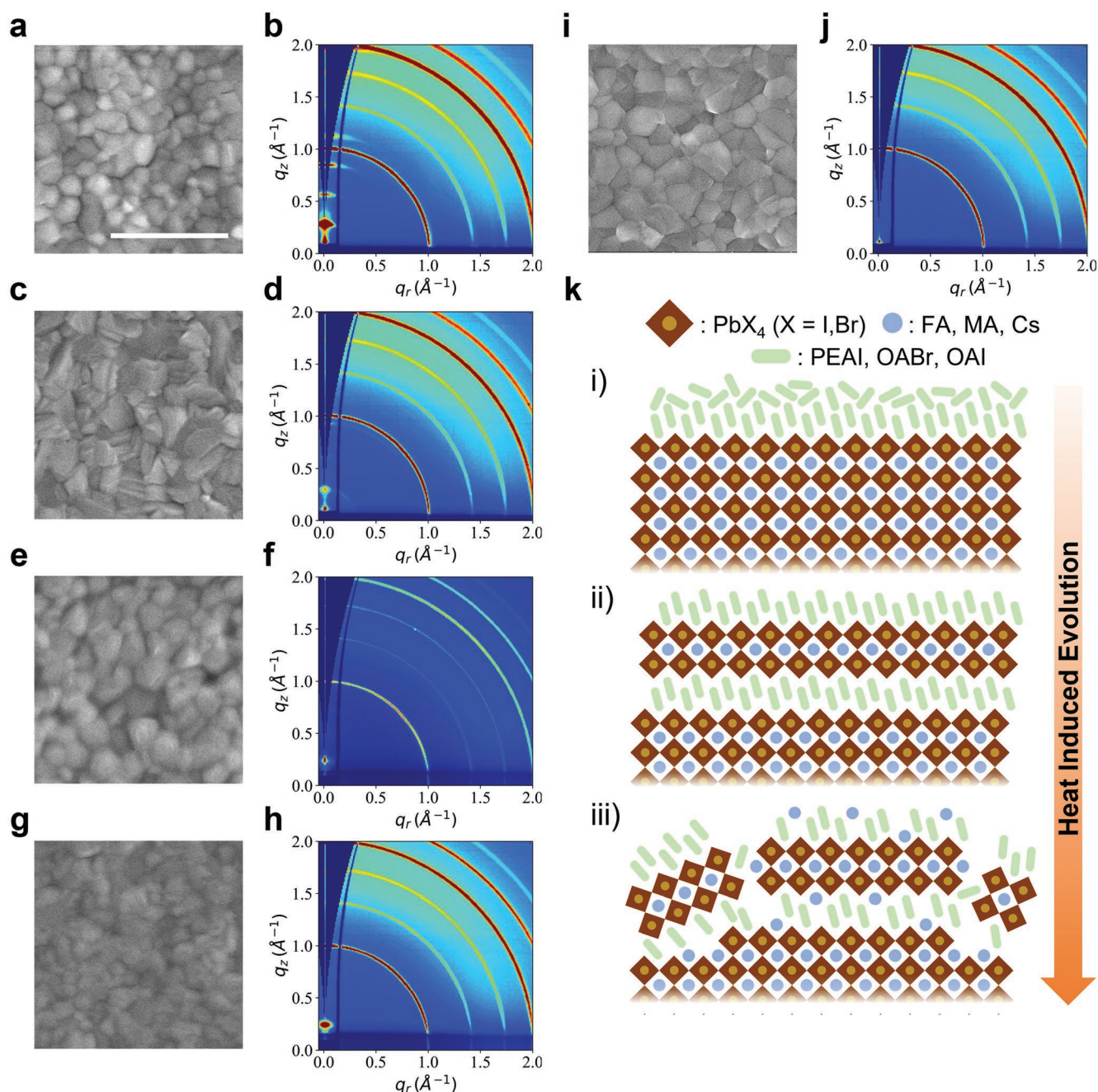
Figure 2. Microstructure and crystal structure evolution of bulky-cation-treated interfaces. a–j) SEM and GIWAXS images of PEAI-treated perovskite films before (a,b) and after (c,d) 40 min annealing; OABr-treated films before (e,f) and after (g,h) annealing; and reference CsFAMA film (i,j). Scale bar for the SEM images is 1 µm. k) Schematics of the evolution of the interface treated with bulky cations upon annealing: i) Formation of an organic overlayer; ii) bulky cation diffusion and RP phase formation; iii) RP reconstruction.

of a crystalline phase even before annealing, with scattering at $q = 0.28$, 0.56, 0.84, 1.13 Å^{-1}, which is absent in the bare CsFAMA film presented in Figure 2j. We attribute those peaks to an RP phase of the type $(PEA)_2(A)_{n-1}Pb_nI_{3n+1}$ with $n = 2$, where A could be Cs, FA, MA.[18,19] All peak maxima belonging to the $(00h)$ family of planes ($h = 1,2,3,4$) are distributed along q_z with regular spacing, indicative of diffraction planes oriented parallel to the sample surface, which is normally the case for RP metal halides. A peak characteristic of PEAI is also observed at 0.35 Å^{-1} in the treated films before annealing, indicating the

presence of an unreacted organic at the surface. Annealing of the PEAI-treated films leads to a structural rearrangement of the interface. Figure S9 in the Supporting Information presents the sector averages along q_z ($-20 < \chi < 20$) and the azimuthal integration of the most intense peak of the RP phases as retrieved from the scattering patterns. For PEAI, we observe a spread in the orientation of the RP phase without loss in the overall peak intensity within the first 10 min at 100 °C, and the disappearance of the peak associated with unreacted PEAI at the surface.

As the annealing time increases to 40 min, loss in crystallinity of the $n = 2$ phase is observed. At the same time, new peaks at larger q values of 0.30, 0.61, 0.93 Å^{-1}—beginning to appear already in the scattering plots for the 10 min annealed films—increase in intensity. The shift of the peak positions toward larger q is indicative of a reduction in the interplanar spacing, however, the shift appears too small to be attributed to a pure transition to an RP phase with $n = 1$, and too large to be merely ascribed to a change in halide or A site composition of the $n = 2$ phase.[20–23] Based on our XPS results showing an increased amount of FA at the surface, we hypothesize that the new peaks might be generated by partial substitution of PEA with FA in $(PEA)_2(A)_1Pb_2I_7$. The orientation of the RP phase decreases further after 40 min of annealing, which could be either related to increased diffusion in the bulk or to a transformation of the surface layer happening in parallel with the loss in crystallinity of the $n = 2$ phase. Based on the depth-dependent GIWAXS study presented in Figure S10 in the Supporting Information, we believe both effects to be present in our films. We probed the bulk and the surface of the films using different incidence angles for the X-rays ($\alpha_{incident} = 0.05$, 0.5), corresponding to penetration depths of 3 and 230 nm (Figure S10a, Supporting Information). In Figure S10b in the Supporting Information, we plot the bulk/surface peak area ratio of the $n = 2$ 001 RP peak. This allowed us to disentangle diffraction signal coming from the bulk or the surface of the films. As shown in Figure S10b in the Supporting Information, annealing causes increased diffraction from the bulk, with a fourfold increase in the bulk/surface signal from the RP phase in the bulk for the film annealed 40 min with respect to the unannealed PEAI-treated sample. At the same time, the azimuthal integration of the 001 peak shows changes from surface to bulk for the film annealed 40 min. A broadened diffraction is seen at the surface, indicative of a loss of orientation in the film which correlates with the loss in crystallinity of the surface RP layer.

In OA-treated films, no crystalline features are visible before applying thermal stress, as shown in Figure 2f and Figure S9 in the Supporting Information, supporting the hypothesis of the amorphous nature of the treated interface before annealing. After annealing for 40 min at 100 °C, a weak signal appears in the diffraction in Figure 2h for both OABr and OAI-treated films (Figure S8, Supporting Information), with planes at $q = 0.25$, 0.49, 0.73 Å^{-1} oriented along q_z which are highlighted in Figure S9 in the Supporting Information. Such scattering features can be all related to the formation of an $n = 2$ RP phase analogous to the case of PEAI.[24,25] The peaks are more intense for the OAI-treated films than for the OABr-treated samples, as evidenced by comparing the sector averages in Figure S9 in the Supporting Information. For the films treated with OA, no secondary phase formation is observed, except for an OABr film showing low-intensity peaks at q of 0.52 and 0.78 Å^{-1} in Figure S9 (Supporting Information) sector average, which suggests an evolution toward structures with smaller interplanar spacing also for this cation, but over significantly longer timescales than PEAI. We note that the RP crystallinity in unannealed PEAI films can vary from batch to batch but evolves toward the same quasi-steady-state after 40 min of annealing. We observed both increases and decreases in the intensity of the RP diffraction

signal within the first 10 min at 100 °C, as shown in Figure S11 in the Supporting Information. Such variability underlines the highly unstable nature of some of the interfaces treated with bulky cations before annealing and the importance of heating the substrates after the deposition of the organic salts to stabilize these structures.

Combining the XPS, SEM, and GIWAXS findings, we can identify: 1) a correlation between the type of bulky cation used and the stability of the treated interface and 2) the evolution stages of the treated interface independent of the type of cation used. Three main transformation steps can be identified, which are depicted in Figure 2k. i) The formation of an organic overlayer: the bulky cations form an overlayer on top of the perovskite film, and only the very interface undergoes conversion. ii) Bulky cation diffusion and RP phase formation: as heat is provided, the cations diffuse in the perovskite layer, inducing interface reconstruction into RP phases. This step proceeds at room temperature for PEAI, as also corroborated by the observations in Figure S11 in the Supporting Information. iii) RP reconstruction and crystallinity loss: after the diffusion step, the composition of the interface layer stabilizes but the structural change continues. New low-dimensional phases with smaller interplanar spacing are formed, and an overall loss in crystallinity is observed. All the data acquired from the three techniques highlight higher thermal stability of the OABr and OAI-treated interfaces with respect to PEAI.

2.3. Bulky Cations Induce Electronic Traps under Thermal Stress

Having understood the evolution in composition and structure of the treated interface, we investigated how the addition of bulky cations affects the stability of the optoelectronic properties of perovskite films and devices. By looking at the trPL decays of CsFAMA films treated with organic salts before and after annealing, we can correlate the structural and chemical changes of the interface with changes in charge-carrier recombination dynamics. As can be seen in **Figure 3**a,b, the annealing process and the solvent used for the deposition of the organics do not affect the PL dynamics in the film, with the CsFAMA perovskite washed with isopropanol (IPA) and annealed showing slightly reduced nonradiative recombination. Differences are observed in Figure 3c,d once the bulky organic cations are deposited on the top perovskite surface (see Figure S12, Supporting Information for OAI-treated films). The charge-carrier lifetimes in the films do not necessarily show clear changes before annealing, as shown in Figure S13 in the Supporting Information, however, annealing of the treated films always results in faster PL decays. The change in carrier dynamics could be ascribed to either increased nonradiative recombination due to the formation of deep traps at the interface or to the extraction of the charge carriers into the newly formed RP phases, followed by recombination across the interface. This trend implies that the reconstruction of the perovskite interface promoted by annealing after bulky cation treatment is detrimental to the quality of the film and will cause PCE loss, as is demonstrated above.

We further studied the effect that the bulky cation treatment and annealing have on the defect population via ECPL. It is
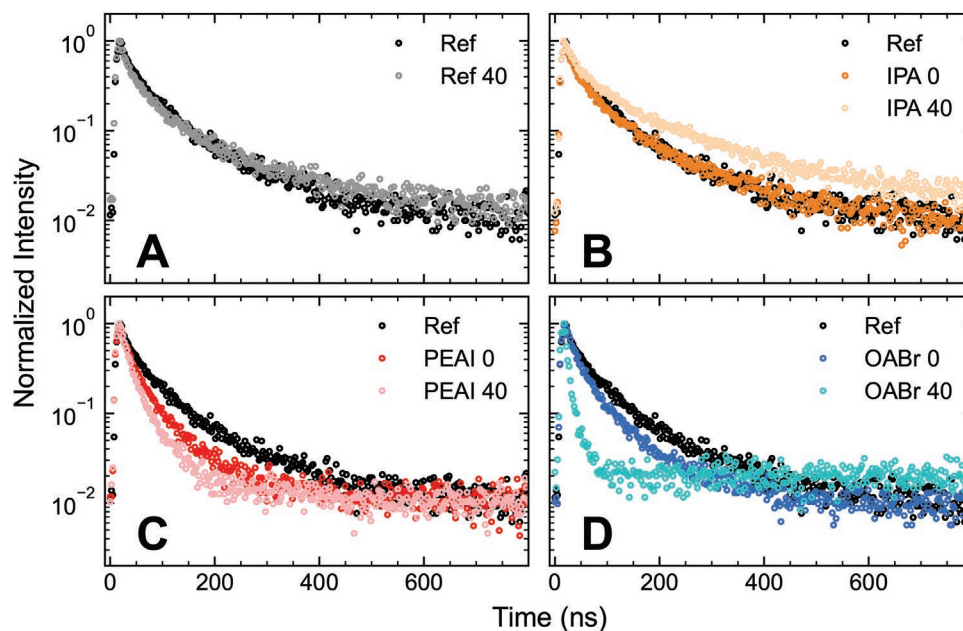
Figure 3. Impact of bulky cations on PL radiative lifetimes. A–D) Time-resolved PL of CsFAMA reference films (A); CsFAMA films washed with IPA to decouple the impact of bulky cations and solvents (B); and CsFAMA films treated with PEAI (C) or OABr (D). All films were measured before and after an annealing step at 100 °C for 40 min. Measurements were performed with a pulse fluence of 66 nJ cm^{-2}.

important to note that in ECPL we are not measuring the PL decay in time, we observe the nonlinear contribution demodulated from the integrated PL. In turn, the time evolution of the ECPL signal corresponds to the evolution of the charge-carrier population after the first pulse, similar to the well-established pump-probe spectroscopy. Further details on the instrumentation and data acquisition can be found in the Experimental Section. The nonlinear contributions to PL, under the Shockley–Read–Hall model, are mainly caused by nonradiative recombination mediated by defects or by Auger recombination processes.[26,27] Defect-assisted nonradiative recombination produces a positive ECPL signal, whereas Auger processes result in a negative ECPL component.[26,27] The opposite sign of the ECPL response between the distinct processes allows a straightforward determination of the main nonradiative recombination pathway. The transition between positive and negative ECPL signal at time zero indicates if the nonradiative recombination is being dominated by trap-assisted or Auger recombination. The ECPL signal of the three films in **Figure 4**a–c undergoes a negative shift as the excitation density increases, which can be attributed to Auger recombination dominating the carrier dynamics as the traps in the perovskite films saturate. A faster transition to Auger processes is indicative of an increased number of free carriers. Therefore, the cross point from positive to negative values can be used as a relative probe of the defect density in the sample. At lower fluences, there is little temporal evolution of the nonlinear carriers, as described by Kandada et al., corresponding to a case well described by deep traps.[27] The lack of temporal evolution arises from slow recombination dynamics, which range from nanoseconds to microseconds, and are outside the time resolution of the equipment. As the incident fluence increases the ECPL signal shifts to negative values and starts to show a decay in the subnanosecond

range, which agrees with what is expected for Auger recombination dominating the population dynamics.[26,28]

Comparing the ECPL response at time zero of the CsFAMA reference film in Figure 4d with the PEAI solution-treated layer in Figure 4e, we observe a clear difference between the fluences at which Auger recombination becomes the main nonradiative path. The cross point from positive to negative ECPL signal is estimated at a fluence of 15 μJ cm^{-2} in the CsFAMA film, while the cross point of the PEAI-treated sample is around 90 μJ cm^{-2}. This change in the cross point implies an increase in the density of traps in the film treated with the PEAI solution. In the ECPL response of the sample treated with PEAI and annealed 40 min, the number of traps gets reduced, but remains still greater than in the reference, as evidenced by a 2% higher response at the lowest fluence (at time zero) and by the cross point to negative ECPL values at 50 μJ cm^{-2}. The ECPL results for the surface-treated film without annealing differ from what is observed in trPL. We hypothesize the change in dynamic to stem from: i) a different fluence used in the two measurements; ii) a high halide concentration at the surface of the PEAI-treated film before annealing; iii) a different atmosphere used for the two measurements. The trPL is performed with a fluence of 66 nJ cm^{-2} (≈10^{15} cm^{-3}) to avoid trap saturation, while the ECPL experiments are performed in a range of 20–350 μJ cm^{-2} (≈10^{17} to 10^{19} cm^{-3}) to saturate traps and be thus able to see nonlinear effects. The (I+Br)/Pb ratio retrieved from XPS in Table S1 in the Supporting Information increases from 4.04 for the reference to 7.65 for the PEAI-treated film with no post-annealing. Upon annealing, the (I+Br)/Pb surface ratio decreases to 5.07. The change in halide composition at the surface is related to the reconstruction of the surface, with a smaller contribution due to evaporation, as evidenced by the XPS measurements on a CsFAMA film with no surface treatment exposed to the
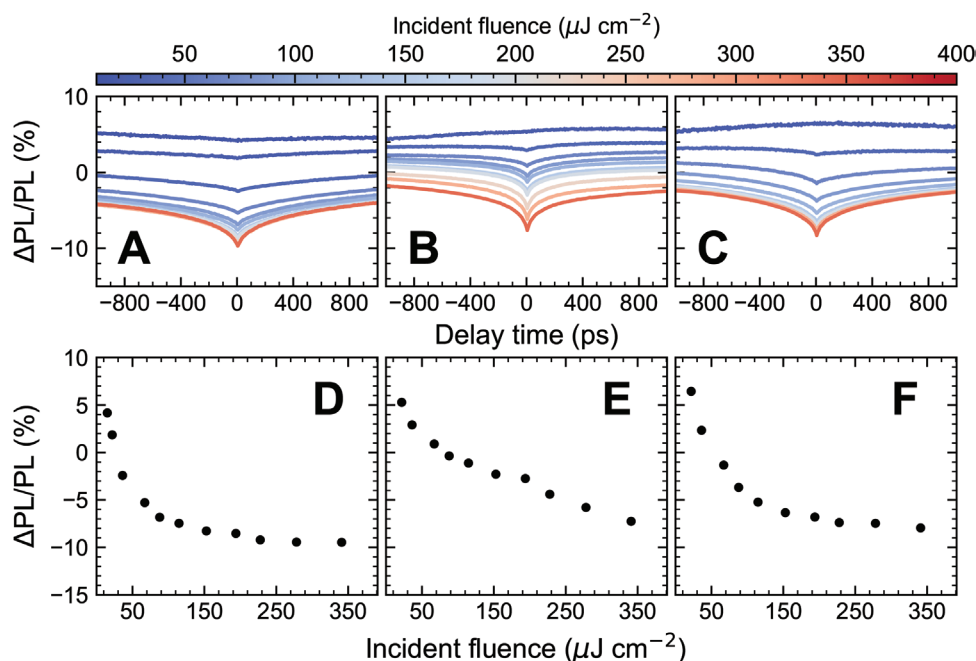
Figure 4. Effect of PEAI treatment on defect density using ECPL. A–F) ECPL dynamics and excitation density dependence of the ECPL at time zero of CsFAMA film (A,D), CsFAMA film treated with a PEAI solution (B,E), and CsFAMA film treated with a PEAI solution annealed for 40 min (C,F).

40 min annealing at 100 °C (Figure S4, Supporting Information). Although treatment with iodine has been used to passivate defects related to iodine deficiency, recent work suggests that an excess of iodine in the surface of lead halide perovskite films can result in the subsequent generation of both shallow and deep traps, a process that is influenced by illumination and presence of oxygen during the measurement.[10,29–32] In particular, iodine defects have been pinpointed as recombination active centers in vacuum conditions, while oxygen presence has been associated with their almost complete passivation.[32] Based on these considerations, we attribute the difference in recombination dynamics between the reference and the PEAI-treated films (Figure 4a,b,d,e) before and after annealing to a change in trap population. Right after interface treatment, we hypothesize the formation of interstitial iodine traps, which can be passivated if oxygen is present during the measurement. Upon annealing, we speculate that the distribution or type of traps dominating the optical response of the film changes (e.g., diffusion in/evaporation of iodine from the film, or formation of traps into the RP phase induced by the loss in crystallinity), with an increase in recombination observed both in trPL and ECPL regardless of the atmosphere used during the measurement.

2.4. Bulky Cations Lower Solar Cell Performance under Thermal Stress

To understand how the evolution of the interface impacts the performance of a complete solar cell, we fabricated devices based on the architecture glass|FTO|TiO$_2$-c|TiO$_2$-mp|CsFAMA|spiro-OMeTAD|Au, as illustrated in Figure 1a, where FTO is fluorine-doped tin oxide, TiO$_2$-c is a compact layer of titanium

dioxide, TiO$_2$-mp is a thin film of TiO$_2$ nanoparticles, and spiro-OMeTAD is 2,2′,7,7′-tetrakis(N,N-di-p-methoxyphenyl-amine)9,9′-spirobifluorene. We focused on studying the PEAI and OABr molecules only, given the similar behavior of OABr and OAI treatments. When included, the organics were deposited on top of the CsFAMA layer, before spiro-OMeTAD. The results are from devices measured 3 days after deposition of the Au electrode as all solar cells—the CsFAMA nontreated reference in particular—showed enhancements in open-circuit voltage (V_{oc}) and short-circuit current (J_{sc}) within this timeframe, as proven in Figure S14 in the Supporting Information. Further, hysteresis decreased significantly in all the devices with aging, suggesting reduced ion motion and/or better energy alignment at the interfaces. The reverse current–voltage scans ($J–V$) of the champion devices for each variation are reported in Figure S15 in the Supporting Information. The distributions of V_{oc}, J_{sc}, fill factor (FF), and stabilized PCE of the devices are reported in **Figure 5**a–d. The choice of reporting the stabilized PCE was taken to screen the effects of hysteresis in the devices and to enable a more direct comparison with reported literature results.[5,6] The medians and standard deviations of the photovoltaic parameters are summarized in **Table 1**. As seen in Figure 5d, the introduction of a bulky organic salt at the CsFAMA interface leads to a small increase in the average stabilized PCE if the films are not exposed to thermal stress, benefiting from reduced hysteresis with respect to the reference (Figure S16, Supporting Information). The PCEs decrease when the bulky-cation layers are annealed, with the largest drop shown in the devices that include PEAI. No clear correlation between hysteresis and annealing was found, as highlighted in Figures S14 and S16 in the Supporting Information. The performance loss induced by annealing is significantly reduced if bulky cations are not used at the interface (Figure S14,
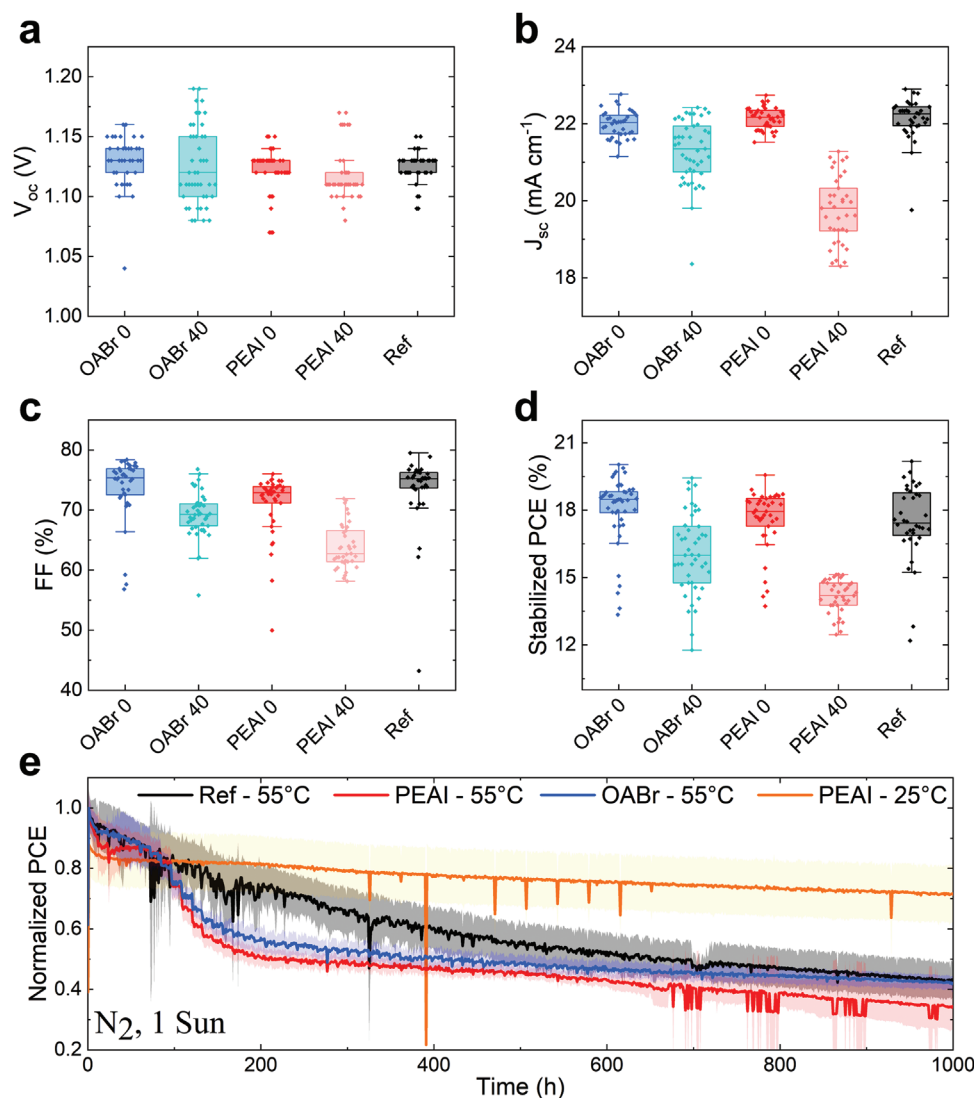
ADVANCED
SCIENCE NEWS

www.advancedsciencenews.com

ADVANCED
MATERIALS

www.advmat.de

Figure 5. Solar cell photovoltaics parameters and stability of solar cells with different surface treatments. a–c) V_{oc}, J_{sc}, and FF distributions as extracted from the reverse J–V scan. d) PCE value after maximum power point tracking for >1 min. More than 36 independent solar cells were fabricated for each variable to produce the boxplots in (a)–(d). Boxplots shaded area includes the 25th to the 75th percentile of the data. Median data value is presented as solid line in the plot. e) Maximum power point tracking under equivalent 1 sun illumination in N_2 atmosphere, 55 °C of the untreated CsFAMA film versus the devices treated with PEAI or OABr without any further annealing. Data are averaged from the stability of five independent solar cells. Three solar cells were averaged for the PEAI–25 °C condition. Average is presented as a solid line, standard deviation as shaded area.

Supporting Information). The decrease in PCE is induced by a simultaneous loss in the median V_{oc}, FF, and J_{sc} values when the organic-treated films are annealed, as seen in Figure 5a–c. We hypothesize two different processes inducing such losses: i) an increased thickness of the interface layer induced by the diffusion of the organic cation and by the conversion of the perovskite interface to low-dimensional phases; ii) the presence of nonpassivated electronic traps in the treated films that are annealed. Process (ii) in particular could lead to the simultaneous drop in the V_{oc}, FF, J_{sc} of annealed devices, whereas an increase in series resistance (i) would only impact FF and J_{sc}. Both effects appear to be present in PEAI devices, as evidenced by the increase in series resistance in dark J–V scans in Figure S17 in the Supporting Information, the trPL trends shown in Figure 3, the ECPL results in Figure 4, and by the V_{oc} trends in

Figure S18 in the Supporting Information. Both (i) and (ii) keep progressing after the first 10 min of annealing (Figure S18, Supporting Information), raising concerns on the long-term operational stability of perovskite layers treated with these cations. No evident contribution from the series resistance in OABr-treated films is observed in Figure S17 in the Supporting Information, suggesting a performance decay mostly dominated by (ii). The V_{oc} drop observed in both types of devices could be induced by the excess halide introduced with the deposition of the organic salts, resulting in the formation of I_i-mediated trap centers.[10,30,31]

As can be seen in Figure 5a, the highest V_{oc}s are reached by films including organic cations and annealed for 40 min, despite the drop in the median V_{oc} values (Table 1), reaching a maximum of 1.19 V for the OABr samples and of 1.17 V for

Table 1. Photovoltaic parameters. Median and standard deviations of photovoltaic parameters extracted from $J-V$ scans in reverse (Rv, bias changing from positive to negative value) and in forward direction (Fw, bias changing from negative to positive value). The stabilized PCE distribution after >1 min maximum power point tracking is reported in the rightmost column. In bold the PCE of the champion devices for each variation.

		V_{oc} [V]	J_{sc} [mA cm^{-2}]	FF [%]	PCE [%]	Stabilized PCE [%]
OABr 0	Rv	1.13 (±0.02)	22.0 (±0.3)	75.4 (±5.4)	18.8 (±1.5)	18.4 (±1.5) **20.0**
	Fw	1.09 (±0.03)	21.9 (±0.4)	70.3 (±3.9)	16.8 (±1.3)	
OABr 40	Rv	1.12 (±0.03)	21.4 (±0.8)	69.3 (±3.8)	16.7 (±1.5)	16.0 (±1.8) **19.4**
	Fw	1.08 (±0.03)	21.3 (±0.9)	67.5 (±3.2)	15.3 (±1.4)	
PEAI 0	Rv	1.13 (±0.02)	22.2 (±0.3)	72.9 (±5.2)	18.1 (±1.4)	17.9 (±1.4) **19.6**
	Fw	1.09 (±0.02)	22.0 (±0.3)	67.7 (±3.8)	16.3 (±1.0)	
PEAI 40	Rv	1.11 (±0.02)	19.8 (±0.9)	62.8 (±3.8)	14.0 (±1.2)	14.2 (±0.7) **15.1**
	Fw	1.07 (±0.02)	19.0 (±0.9)	62.8 (±1.5)	12.9 (±0.6)	
Ref	Rv	1.13 (±0.01)	22.2 (±0.5)	75.2 (±6.2)	18.7 (±1.7)	17.4 (±1.7) **20.2**
	Fw	1.07 (±0.02)	22.0 (±0.6)	65.9 (±5.9)	15.5 (±1.6)	

the PEAI, against the 1.15 V of the reference. This contradictory result can be explained by noting that a V_{oc} enhancement is also observed in the CsFAMA reference exposed to 40 min extra of annealing in Figure S14 in the Supporting Information (see devices remeasured 3 days after Au deposition). Heterogenous coverage of the organic layer might thus result in a dominance of the V_{oc} enhancement effect of annealing and explain the presence of outliers. The increase in the heterogeneity of the film with 40 min of annealing extends beyond the surface. X-ray fluorescence (XRF) maps were acquired to track the in-plane spatial distribution of halides in the film as a function of surface treatment and annealing. The XRF maps presented in Figure S19 in the Supporting Information show increased halide heterogeneity (Br:Pb, mol:mol) in the treated perovskite films after 40 min of annealing. The small change in performance observed between the reference device and those treated with the bulky cations with no annealing contradicts some of the results already published.[5] Such difference might stem from an excess of FA at the surface acting to passivate defects in our films, as previously reported for similar formulations.[13] We note that in a batch we observed higher PCEs for the devices treated with PEAI and OABr with respect to the reference, even after 3 days, leading us to hypothesize that if there are problems with the active layer or at the perovskite|charge-transport-layer interface, the use of a top-interface modifier can lead to an efficiency enhancement. However, as shown in Figure S20 in the Supporting Information, the drop in performances with annealing was observed even in such cases. These same dynamics apply to different perovskite compositions, as shown in Figure S21 in the Supporting Information for $Cs_{0.09}FA_{0.91}PbI_3$ perovskite devices. Further, these dynamics are expected to happen regardless of the quality of the metal halide perovskite layer.[4] As such, we believe the dynamics here described to be of general application to bulky cation-treated films. The interface treatment can have a positive effect without annealing, but annealing causes a significant drop in performance with some of the bulky cations commonly used. Reducing the bulky cation concentration to offset the annealing effect is not a solution. Figure S22 in the Supporting Information shows how the drop in efficiencies is still observed at 10×10^{-3} M (2.5 mg mL^{-1}). Further decreasing the bulky cation

concentration to 5×10^{-3} M (1.25 mg mL^{-1}) causes the PCE to drop with respect to the reference, with recovery after 40 min of annealing. We speculate that at such low concentration, the PEAI wash resembles an IPA wash of the surface of the 3D perovskite, with a negligible amount of bulky cation left at the interface.

We investigated if the transformative dynamics observed in interface-modified perovskite films were also observed during solar cell operation. We thus exposed the solar cells to 1 Sun equivalent illumination at 55 °C in an inert atmosphere and used a maximum power point (MPP) tracking algorithm to monitor the decay in their PCE. Every 12 h, we performed a $J-V$ scan to retrieve the evolution in J_{sc}, FF, V_{oc} during aging. Figure 5e presents a comparison of the stability of the untreated device versus solar cells including a PEAI or OABr layer. Figure S23 in the Supporting Information reports the results of the photovoltaic parameters extracted from the $J-V$ scans. Figure S24 in the Supporting Information includes a comparison of the stability of treated devices aged at 25 °C versus 55 °C. In Figure 5e, after the first 100 h of stress testing, surface-treated devices experienced a marked performance decrease not observed in the reference. We associate this decay with the transformation of the interface treated with bulky cation impacting charge extraction, as also corroborated by the strong drops in J_{sc} and FF observed in Figure S23 in the Supporting Information, which resembles the losses observed in films treated with PEAI and annealed 40 min at 100 °C. While the exact structure of the interface might differ in this case from the structure observed in devices annealed at 100 °C, the absence of a rapid efficiency decay in devices with no bulky cation treatment highlights clearly that the performance drop is driven by transformative processes introduced by the bulky cations. The rapid MPP decay in surface-treated films significantly slows after the first 200 h of light exposure, suggesting that further performance degradation might be hindered once the interface treated with bulky cations reaches its most thermodynamically stable configuration. The MPP traces for PEAI and OABr films differ slightly. In PEAI-treated films, a PCE drop with respect to the reference is observed within the first 50 h of illumination, which is not present when OABr is used. After 200 h of stressing, the efficiency loss proceeds with the

same slope as the reference film in PEAI. Instead, for OABr the MPP stabilizes almost completely. While it is not possible to draw a direct correlation between the different MPP dynamics and the interface evolution observed with optical and surface measurements, the observed trends reinstate the need to test bulky cation-treated films at high temperatures, show differences dependent on the cations used and, as here in the case of OABr, the possibility to provide a stable MPP after an initial annealing step is completed. As shown in Figure 5e, in the case of PEAI, temperature has a key role in the stability of interface-treated devices. If PEAI-coated films are kept at 25 °C during the stability measurement, no PCE drop is observed. To further corroborate the functionality of our surface treatment protocol, we exposed perovskite films with and without a top bulky cation layer to ambient conditions for 14 days, under ≈70% relative humidity. As can be seen in Figure S24 in the Supporting Information the bulky cations successfully prevented the degradation of the perovskite layer in humid air conditions, preserving the typical dark coloration of the CsFAMA layer. However, surface-treated films with 40 min annealing saw degradation similar to that of the reference, providing evidence that the cation diffusion leads to inefficient protection of the bulk of the perovskite.

3. Conclusion

We have investigated the thermal stability of bulky cation layers based on organic salts such as PEAI, OAI, and OABr, which have been frequently used to treat surfaces of perovskite films for defect passivation in optoelectronic applications. We demonstrated the vulnerability of these interface layers. Upon annealing at 100 °C, bulky cations diffuse in the perovskite layer, cause changes in the structure and crystallinity of the interface, and become less effective as barriers against the effects of oxygen and moisture. This evolution affects the optoelectronic properties of the film. The deposition of the bulky cations introduces excess halides at the surface that do not contribute to recombination, possibly owing to passivation of these defects when measurements are carried out in air. Upon annealing, the type of defects dominating nonradiative recombination is changed, resulting in decreased performances. The PCE drop can be observed also during device operation in the form of a sudden decrease in performances within the first 200 h of MPPT, even when experiments are carried out at mild temperatures of 55 °C. The performances of films treated with bulky cations seem to stabilize after the initial drop in performances in Figure 5. This suggests that once interfaces treated with bulky cations reach a thermodynamically stable state, device lifetime could be extended. Regardless, testing at high temperature will be required to ensure screening of these instabilities, given that these degradation dynamics are hidden at $t = 0$ or low temperatures. This makes measuring thermal stability even more important in devices treated with bulky cations. Based on our findings, we propose that developing molecules that do not reconstruct the perovskite film surface and using nonhalide counterions when performing the bulky cation treatment might overcome these stability limitations, benefiting the PCE and long-term operation of perovskite photovoltaics. Such observations stress the need for new bulky-cation modi-

fiers that withstand thermal stress and the need to test devices at temperatures ≥55 °C to ensure reporting performances and stability relevant for photovoltaic operation.

4. Experimental Section

Perovskite Solution Preparation: To prepare the $Cs_{0.06}MA_{0.16}FA_{0.79}PbI_{2.52}Br_{0.49}$ (CsFAMA) perovskite solution, $PbBr_2$ (Tokyo Chemical Industry—TCI) and PbI_2 (TCI) were dissolved in separate vials using a 4:1 volume ratio of dimethyl formamide:dimethyl sulfoxide (DMF:DMSO, Sigma Aldrich) to form a 1.5 M solution of each. The solutions were stirred and heated to 60 °C for 1 h. Once cooled down, the Pb precursor solutions were added to formamidinium iodide (FAI, Dynamo) and methylammonium bromide (MABr, Dynamo) powders, respectively, to obtain 1.24 M $FAPbI_3$ and $MAPbBr_3$ solutions with 5% Pb excess. The prepared solutions were then mixed in a 17:83 volume ratio (MAFA solution). The MAFA solution was subsequently mixed with a 1.5 M CsI (Sigma Aldrich) solution in DMSO in a 95:5 volume ratio. For $Cs_{0.09}FA_{0.91}PbI_3$ (CsFA) mixed-cation perovskite, 1.2 M of CsFA perovskite solution was prepared with an excess Pb of 5%. The PbI_2 powder was first mixed in 2:1 volume ratio of DMF:DMSO and then dissolved at 85 °C for 20 min. After the PbI_2 precursor solution was cooled, it was added to the FAI and CsI powders. All the procedures were completed in a nitrogen glovebox.

Solar Cell Fabrication: 1 in x 1 in Patterned glass|FTO (7 Ω sq^{-1}) substrates were cleaned by sonication 15 min in a 2% Hellmanex solution, followed by 10 min sequential steps in deionized water, acetone, and isopropanol. Substrates were immediately dried with a nitrogen gun and positioned on a hotplate for the subsequent deposition of the electron-transport layer. The edges of each substrate were covered with glass slides, leaving the active area of the pixels uncovered, and the temperature of the hotplate was set to 450 °C. A compact layer of TiO_2 (TiO2-c) was then deposited by spray pyrolysis, using a solution comprising 480 µL of acetylacetone (Sigma-Aldrich), 720 µL of titanium di-isopropoxide bis(acetylacetonate) (75% in 2-propanol, Sigma-Aldrich), and 10.8 mL of 99.9% pure anhydrous ethanol (Sigma-Aldrich). A 3.5 L min^{-1} flow of oxygen was used as carrier gas to spray the solution. A Sparmax spray gun was used for spray, using ≈10 s passages with 30 s delay between each cycle. The spray was continued until the solution was finished. The substrates were then kept at 450 °C for 30 min and let cooled down to room temperature. The mesoporous TiO_2 film (TiO2-mp) was spin-coated from a 150 mg mL^{-1} solution of TiO_2 paste (30 nm nanoparticles, GreatSolar) in ethanol (99.9% pure, anhydrous, Sigma-Aldrich). Spin-coating parameters were 2000 rpm, 2000 rpm s^{-1}, 10 s. Magic tape was used to prevent deposition on the contacts of the mesoporous solution during spin coating. The deposited substrates were immediately moved to a hotplate at 100 °C for drying (>10 min). The mesoporous film was subsequently sintered by slowly carrying the substrates at 450 °C and maintaining the temperature for 30 min. Substrates were removed from the hotplate after partial cool down, while still at ≈150 °C, and immediately transferred to a glovebox with <10 ppm O_2 and H_2O. The CsFAMA solution was then deposited using a solvent quenching protocol. Namely, 45 µL of CsFAMA solution was deposited on the TiO_2 covered substrates and then spun at 1000 rpm, 10 s, followed by 6000 rpm, 20 s. 250 µL chlorobenzene (Sigma-Aldrich, anhydrous) were dripped (≈1 s duration) 5 s before the completion of the second step. The N_2 supply to the spin-coater was kept off during deposition to minimize solvent re-evaporation from the walls of the spin-coater. The samples were then annealed at 100 °C for 30 min. If the CsFA solution was used, it was deposited using the same two-step spin-coating procedure mentioned above with the following modifications: 90 µL of CsFA solution used, 250 µL of chlorobenzene used for quenching dropped 3 s before the end of the second spin-coating step, and annealing performed at 150 °C for 10 min. For the interface treatment, 20×10^{-3} M solutions of either PEAI, OAI, OABr in 2-propanol (anhydrous, Sigma-Aldrich) were dynamically spin-cast

**ADVANCED
SCIENCE NEWS**

www.advancedsciencenews.com

**ADVANCED
MATERIALS**

www.advmat.de

on the perovskite film at 5000 rpm, 5000 rpm s^{-1}, 20 s and annealed (when needed) at 100 °C for different time durations. A spiro-OMeTAD 28.4 × 10^{-3} M solution was prepared right before deposition, with the addition of 14.5 µL of Co (II) salt (FK209, Sigma-Aldrich, 300 mg mL^{-1} stock solution in acetonitrile), 8.8 µL of Li-TFSI (Sigma-Aldrich, 520 mg mL^{-1} in acetonitrile stock solution), and 14.4 µL of *tert*-butylpyridine (Sigma-Aldrich). Spin-coating parameters were 3000 rpm, 3000 rpm s^{-1}, 30 s. 80 µL spiro-OMeTAD solution were dripped on the substrate ≈1 s after spin-coating start. The edges of the substrates were cleaned from the CsFAMA and spiro-OMeTAD films before Au deposition, using cotton swabs wet with DMF and acetonitrile, respectively. Finally, 56 nm of gold were thermally evaporated as top contact for the device.

Thin-Film Characterization: SEM images were acquired using a Hitachi SU8230 using a secondary-electron detector at 5 keV and 9 µA emission current. GIWAXS images were acquired at beamline 11-BM, Brookhaven national laboratory, on perovskite films deposited on glass|ITO substrates reduced to about 0.5 cm × 0.5 cm size for the measurement. Images were acquired at an impinging angle α of 0.5° with 10 s exposure time, using an X-ray beam energy of 13.5 keV, and 0.2 mm (height) × 0.05 mm (width) size. Beam divergence was 1 mrad and energy resolution 0.7%. Data analysis was performed building on the SciAnalysis package provided by the beamline. XPS measurements were taken on a Thermo Scientific K-Alpha X-ray photoelectron spectrometer. Survey scans were acquired averaging two measurements with 200 eV pass energy and 1 eV energy step size. Elemental scans were acquired using 50 eV pass energy and 0.1 eV energy step size. 10 scans were used for Br, 5 for Pb, 15 for C, 10 for N, 15 for O, 4 for I, and 10 for Cs. The Pb-X peak position was used to reference the binding energies for the different samples, as the content of organics in the films made the use of the C—C peak position from contaminants unreliable. The elemental composition analysis was performed using the Thermo Scientific Avantage data system for surface analysis. trPL measurements were performed using an ultrafast laser system (Pharos Model PH1-20-0200-02-10, Light Conversion) emitting 1030 nm pulses at 100 kHz, with an output power of 20 W and pulse duration of ≈220 fs. Experiments were carried out in an integrated transient absorption/time-resolved PL commercial set-up (Light Conversion Hera). A 470 nm pump was generated by feeding 10 W from the laser output to a commercial optical parametric amplifier (Orpheus, Light Conversion). The bean radius was estimated by 90/10 knife edge technique to be 155 µm resulting in a pulse fluence of 66 nJ cm^{-2}.

Excitation Correlation Photoluminescence (ECPL) Spectroscopy: A schematic of the ECPL setup is presented in Figure S25 in the Supporting Information. The ECPL instrument was consisted in 1030 nm ≈220 fs pulses generated in an ultrafast laser system (PHAROS Model PH1-20-0200-02-10, Light Conversion) which fed 10 W to a commercial optical parametric amplifier (ORPHEUS, Light Conversion) from which a pump energy of 2.64 eV was selected. The excitation intensity was varied by using a motorized filter wheel (FW212CNEB, Thorlabs). The pulse train was split 50/50 with a beam splitting. One of the beams was directed to a motorized linear stage (LTS300, Thorlabs), allowing a delay control between the two pulses. Each pulse was modulated with a chopper at different frequencies 373 and 217 Hz. The pulses were then focused onto the perovskite sample with a 100 mm focal length lens. The emitted PL was filtered with a 550 nm long-pass and focused in to a photoreceiver. The photoreceiver was connected to a lock-in amplifier (HF2LI, Zurich Instruments) where the total integrated PL and the nonlinear component (ΔPL) were obtained simultaneously by demodulating both at the fundamental and the sum frequency. The perovskite films were measured inside a closed-cycle cryostat (Montana Instruments). Data acquisition: The lock-in amplifier demodulated the photoluminescent signal at three frequencies, ω_1, ω_2, and $\omega_1 + \omega_2$, which give the linear PL contribution from pulse 1, the linear contribution from pulse 2, and the nonlinear contribution, respectively. The lock-in output could be expressed as

$$Z = |R| e^{i\theta} = X + iY \tag{1}$$

Since the PL from pulse 1 and 2 corresponded to positive numbers, the |R| component was used from the demodulated signal. However,

nonlinear contribution could be either positive or negative, the phase was set such that X was maximized and positive. It was verified that X was positive for a particular excitation density and the phase constant was kept through the fluence dependence experiments. The sign was verified by modulating only one of the pulses and comparing it's lock-in response in the presence and absence of the second pulse not modulated (chopper off). If the signal increased with the presence of the second pulse that indicated that the sign was positive, however if it decreased the sign was negative. The ΔPL/PL was obtained from the demodulated signals as

$$\frac{PL}{PL}(\%) = \frac{PL^{demod(\omega_1+\omega_2)} \times 100}{PL^{demod(\omega_1)} + PL^{demod(\omega_2)} + PL^{demod(\omega_1+\omega_2)}} \tag{2}$$

where $PL^{demod(\omega)}$ corresponds to the signal demodulated at the frequency ω.

Device Characterization: The photovoltaic performance was evaluated using a Fluxim Litos Lite setup, equipped with a Wavelabs Sinus-70 AAA solar simulator with AM1.5 spectrum for excitation. The current–voltage (*J*–*V*) characteristics were acquired with forward and reverse scans at a scan rate of 50 mV s^{-1}. The stabilized power output was acquired using an MPP tracking algorithm for 60 s. Devices were not preconditioned before measurement. Masking was used during the measurement, defining a pixel area of 0.0625 cm^2. Nitrogen was flown in the measurement chamber during characterization. No temperature control was applied.

Aging tests were performed using a Fluxim Litos setup, using 1 Sun equivalent illumination with no UV-component, holding the substrates at 55 °C in a N$_2$ atmosphere and using an MPP tracking algorithm. Every 12 h, a *J*–*V* scan in reverse and forward direction was automatically acquired.

Statistical Analysis: Outliers (nonworking pixels) were removed from the *J*–*V* boxplots in Figure 5a–d and Figures S12, S14, S18, and S19 in the Supporting Information by setting a threshold filter at 11% on the stabilized PCE. No preprocessing was performed on data presented in Figures S17 and S21 in the Supporting Information. After removal of the outliers, the performances presented in the boxplots in Figure 5a–d were obtained including data from >36 individual solar cells for each variation. For the boxplots in Figures S12, S14, S16, S18–S20 in the Supporting Information, >12 individual solar cells per condition were averaged. Boxplots presented the median value as a solid line in the box, the bottom and top of the box were the 25th and 75th percentile, respectively. Whiskers were positioned at the 5th and 95th percentile, respectively. Boxplots in Figure 5a–d in the main text were plotted using OriginPro 2022 software, whereas boxplots in the Supporting Information were plotted using the python module "seaborn."

To provide an estimate of error on the stability measurement presented in Figure 5e, the performances of each solar cell were normalized to 1 at $t = 0$, and then averaged. The average was presented as a solid line, while the standard deviation was presented as the shaded area. The stability of five individual solar cells was monitored for each condition.

Supporting Information

Supporting Information is available from the Wiley Online Library or from the author.

Acknowledgements

Conflict of Interest

The authors declare no conflict of interest.

Data Availability Statement

The data that support the findings of this study are available from the corresponding author upon reasonable request.

Keywords

interface passivation, interface structures, perovskite solar cells, stability, surface structures, surface chemistry

[1] C. A. R. Perini, T. A. S. Doherty, S. D. Stranks, J.-P. Correa-Baena, R. L. Z. Hoye, *Joule* **2021**, *5*, 1024.

[2] A. A. Sutanto, R. Szostak, N. Drigo, V. I. E. Queloz, P. E. Marchezi, J. C. Germino, H. C. N. Tolentino, M. K. Nazeeruddin, A. F. Nogueira, G. Grancini, *Nano Lett.* **2020**, *20*, 3992.

[3] G. Yang, Z. Ren, K. Liu, M. Qin, W. Deng, H. Zhang, H. Wang, J. Liang, F. Ye, Q. Liang, H. Yin, Y. Chen, Y. Zhuang, S. Li, B. Gao, J. Wang, T. Shi, X. Wang, X. Lu, H. Wu, J. Hou, D. Lei, S. K. So, Y. Yang, G. Fang, G. Li, *Nat. Photonics* **2021**, *15*, 681.

[4] F. Fiorentino, M. D. Albaqami, I. Poli, A. Petrozza, *ACS Appl. Mater. Interfaces* **2021**, *14*, 34180.

[5] Q. Jiang, Y. Zhao, X. Zhang, X. Yang, Y. Chen, Z. Chu, Q. Ye, X. Li, Z. Yin, J. You, *Nat. Photonics* **2019**, *13*, 500.

[6] J. J. Yoo, G. Seo, M. R. Chua, T. G. Park, Y. Lu, F. Rotermund, Y.-K. K. Kim, C. S. Moon, N. J. Jeon, J.-P. P. Correa-Baena, V. Bulović, S. S. Shin, M. G. Bawendi, J. Seo, *Nature* **2021**, *590*, 587.

[7] G. W. Kim, A. Petrozza, *Adv. Energy Mater.* **2020**, *10*, 2001959.

[8] L. Fu, H. Li, L. Wang, R. Yin, B. Li, L. Yin, *Energy Environ. Sci.* **2020**, *13*, 4017.

[9] H. Kim, S. U. Lee, D. Y. Lee, M. J. Paik, H. Na, J. Lee, S. Il Seok, *Adv. Energy Mater.* **2019**, *9*, 1902740.

[10] S. Tan, I. Yavuz, M. H. Weber, T. Huang, C. H. Chen, R. Wang, H. C. Wang, J. H. Ko, S. Nuryyeva, J. Xue, Y. Zhao, K. H. Wei, J. W. Lee, Y. Yang, *Joule* **2020**, *4*, 2426.

[11] Q. Zhou, L. Liang, J. Hu, B. Cao, L. Yang, T. Wu, X. Li, B. Zhang, P. Gao, *Adv. Energy Mater.* **2019**, *9*, 1802595.

[12] B. Philippe, M. Saliba, J. P. Correa-Baena, U. B. Cappel, S. H. Turren-Cruz, M. Grätzel, A. Hagfeldt, H. Rensmo, *Chem. Mater.* **2017**, *29*, 3589.

[13] T. J. Jacobsson, J. P. Correa-Baena, E. Halvani Anaraki, B. Philippe, S. D. Stranks, M. E. F. Bouduban, W. Tress, K. Schenk, J. Teuscher, J. E. Moser, H. Rensmo, A. Hagfeldt, *J. Am. Chem. Soc.* **2016**, *138*, 10331.

[14] M.-C. Tang, S. Zhang, T. J. Magnanelli, N. V. Nguyen, E. J. Heilweil, T. D. Anthopoulos, C. A. Hacker, *Mater. Adv.* **2021**, *2*, 1253.

[15] Y. J. Hofstetter, I. García-Benito, F. Paulus, S. Orlandi, G. Grancini, Y. Vaynzof, *Front. Chem.* **2020**, *8*, 66.

[16] S. W. Knipe, J. R. Mycroft, A. R. Pratt, H. W. Nesbitt, G. M. Bancroft, *Geochim. Cosmochim. Acta* **1995**, *59*, 1079.

[17] H. Zhu, Y. Liu, F. T. Eickemeyer, L. Pan, D. Ren, M. A. Ruiz-Preciado, B. Carlsen, B. Yang, X. Dong, Z. Wang, H. Liu, S. Wang, S. M. Zakeeruddin, A. Hagfeldt, M. I. Dar, X. Li, M. Grätzel, *Adv. Mater.* **2020**, *32*, 1907757.

[18] D. J. Morrow, M. P. Hautzinger, D. P. Lafayette, J. M. Scheeler, L. Dang, M. Leng, D. D. Kohler, A. M. Wheaton, Y. Fu, I. A. Guzei, J. Tang, S. Jin, J. C. Wright, *J. Phys. Chem. Lett.* **2020**, *11*, 6551.

[19] W. Peng, J. Yin, K. T. Ho, O. Ouellette, M. De Bastiani, B. Murali, O. El Tall, C. Shen, X. Miao, J. Pan, E. Alarousu, J. H. He, B. S. Ooi, O. F. Mohammed, E. Sargent, O. M. Bakr, *Nano Lett.* **2017**, *17*, 4759.

[20] M. E. F. Bouduban, V. I. E. Queloz, V. M. Caselli, K. T. Cho, A. R. Kirmani, S. Paek, C. Roldan-Carmona, L. J. Richter, J. E. Moser, T. J. Savenije, M. K. Nazeeruddin, G. Grancini, *J. Phys. Chem. Lett.* **2019**, *10*, 5713.

[21] Y. Liu, Y. Zhang, Z. Yang, H. Ye, J. Feng, Z. Xu, X. Zhang, R. Munir, J. Liu, P. Zuo, Q. Li, M. Hu, L. Meng, K. Wang, D. M. Smilgies, G. Zhao, H. Xu, Z. Yang, A. Amassian, J. Li, K. Zhao, S. F. Liu, *Nat. Commun.* **2018**, *9*, 5302.

[22] M. E. Kamminga, H. H. Fang, M. R. Filip, F. Giustino, J. Baas, G. R. Blake, M. A. Loi, T. T. M. Palstra, *Chem. Mater.* **2016**, *28*, 4554.

[23] D. Ma, Y. Fu, L. Dang, J. Zhai, I. A. Guzei, S. Jin, *Nano Res.* **2017**, *10*, 2117.

[24] A. Lemmerer, D. G. Billing, *Dalton Trans.* **2012**, *41*, 1146.

[25] Y. Hua, D. Hong, S. Wan, Y. Lei, M. Xie, W. Yang, Y. Du, Y. Tian, *J. Lumin.* **2020**, *220*, 116981.

[26] A. R. Srimath Kandada, S. Neutzner, V. D'Innocenzo, F. Tassone, M. Gandini, Q. A. Akkerman, M. Prato, L. Manna, A. Petrozza, G. Lanzani, *J. Am. Chem. Soc.* **2016**, *138*, 13604.

[27] D. A. Valverde-Chávez, E. Rojas-Gatjens, J. Williamson, S. Jariwala, Y. Shi, D. P. McCarthy, S. Barlow, S. R. Marder, D. S. Ginger, C. Silva-Acuña, *J. Mater. Chem. C* **2021**, *9*, 8204.

[28] G. Xing, N. Mathews, S. S. Lim, N. Yantara, X. Liu, D. Sabba, M. Grätzel, S. Mhaisalkar, T. C. Sum, *Nat. Mater.* **2014**, *13*, 476.

[29] W. Q. Wu, P. N. Rudd, Z. Ni, C. H. Van Brackle, H. Wei, Q. Wang, B. R. Ecker, Y. Gao, J. Huang, *J. Am. Chem. Soc.* **2020**, *142*, 3989.

[30] J. S. Park, J. Calbo, Y. K. Jung, L. D. Whalley, A. Walsh, *ACS Energy Lett.* **2019**, *4*, 1321.

[31] S. G. Motti, D. Meggiolaro, A. J. Barker, E. Mosconi, C. A. R. Perini, J. M. Ball, M. Gandini, M. Kim, F. De Angelis, A. Petrozza, *Nat. Photonics* **2019**, *13*, 532.

[32] S. Kosar, A. J. Winchester, T. A. S. Doherty, S. Macpherson, C. E. Petoukhoff, K. Frohna, M. Anaya, N. S. Chan, J. Madéo, M. K. L. Man, S. D. Stranks, K. M. Dani, *Energy Environ. Sci.* **2021**, *14*, 6320.